



D. Ding¹ and J.B. Bostwick¹,†

¹Department of Mechanical Engineering, Clemson University, Clemson, SC 29634, USA

(Received 18 February 2022; revised 26 May 2022; accepted 29 May 2022)

Drop-on-demand printing applications involve a drop connected to a fluid reservoir between which volume can be exchanged, a situation that can be idealized as a sessile drop with prescribed volume flux across the drop/reservoir boundary. Here we compute the frequency spectrum for these pressure disturbances, as it depends upon the static contact-angle α (CA) and an empirical constant χ relating the reservoir pressure to volume exchanged, for either (i) pinned or (ii) free contact-lines. Mode shapes are characterized by the mode number pair $[k,\ell]$ with property $k+\ell=\mathbb{Z}_{odd}^+$ that can be associated with the symmetry properties of the Rayleigh drop modes for the free sphere. We report instabilities to the axisymmetric [1,0] and non-axisymmetric rocking [2,1] modes that are related to centre-of-mass motions, and show how the spectral degeneracy of the Rayleigh drop modes breaks with the model parameters.

Key words: drops, contact lines, wetting and wicking

1. Introduction

In one of his seminal works, Lord Rayleigh (1879) showed that a free spherical drop held by surface tension will oscillate about its equilibrium shape with characteristic frequency

$$\omega_{k,\ell} = \sqrt{k(k-1)(k+2)\frac{\sigma}{\varrho R^3}} \quad k, \ell = 0, 1, \dots, \infty; \ \ell \leqslant k$$
 (1.1)

and mode shape Y_k^ℓ given by the spherical harmonics of degree k and order ℓ , in what has now become one of the canonical problems in drop dynamics. Here ϱ , σ , R are the density, surface tension and drop radius, respectively. The Rayleigh spectrum (1.1) has stood the test of time having been verified in both terrestrial (Trinh & Wang 1982) and microgravity (Wang, Anilkumar & Lee 1996) conditions. Recent interest in drop oscillations has focused on the role substrate contact has on the frequency spectrum for a variety of wetting conditions (Chebel, Risso & Masbernat 2011; Sharp, Farmer & Kelly 2011; Sharp 2012; Sakakeeny *et al.* 2021). Such drop wetting interactions are typified in the problem of

† Email address for correspondence: jbostwi@clemson.edu

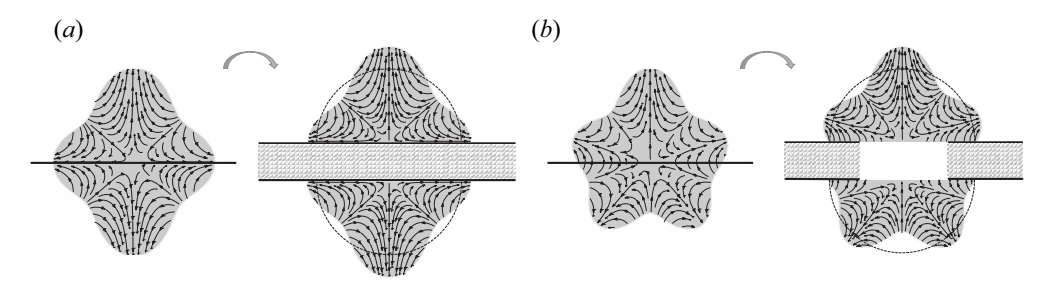


Figure 1. Symmetry decomposition of the Rayleigh drop modes $[k,\ell]$ into sessile-drop modes with (a) even and (b) odd symmetry about the horizontal midplane for $\alpha=90^\circ$. The $k+\ell=\mathbb{Z}^+_{even}$ modes have a contact-line that moves with fixed contact-angle and flow field that naturally satisfies a no-penetration condition on the symmetry plane, whereas the $k+\ell=\mathbb{Z}^+_{odd}$ modes have a pinned contact-line with non-zero flux condition on the symmetry plane.

sessile-drop oscillations. Our interest is in the symmetry decomposition of the Rayleigh spectrum and how it relates to the sessile-drop spectrum.

Bostwick & Steen (2014) have computed the frequency spectrum for the sessile drop on a flat substrate showing how it depends upon the static contact-angle α and contact-line (CL) mobility resistance parameter Λ associated with the 'Hocking condition' (Davis 1980; Hocking 1987). Limiting cases correspond to freely moving $\Lambda=0$ and pinned $\Lambda=\infty$ CLs with intermediate cases $\Lambda\neq 0,\infty$ corresponding to stick-slip behaviours (Shaikeea et al. 2017). We note an analytical-based solution method has recently been proposed by Sharma & Wilson (2021) for pinned drops. The predictions of Bostwick & Steen (2014) have been verified for drops with pinned CLs ($\Lambda=\infty$) by Chang et al. (2013, 2015) over a range of α . The structure of the spectrum is rich and includes predictions such as splitting of the Rayleigh drop degeneracy, spectral reordering and mode mixing, all of which have been verified experimentally. Notably, Steen, Chang & Bostwick (2019) have introduced an organizational structure for the sessile-drop spectrum introducing the 'periodic table of droplet motions'. Their modal classification system is inherited from the Rayleigh drop and restricts mode numbers $k+\ell=\mathbb{Z}_{even}^+$, as required to enforce the no-penetration condition at the solid support.

The Rayleigh drop modes for the full sphere are given by the spherical harmonics and defined by the mode number pair $[k,\ell]$ with $\ell\leqslant k$. Note the spectrum (1.1) is degenerate with respect to azimuthal mode number l. Figure 1 plots the Rayleigh modes with (a) $k+\ell=\mathbb{Z}_{even}^+$ and (b) $k+\ell=\mathbb{Z}_{odd}^+$ and their corresponding symmetry extension about the equatorial plane that defines the hemispherical $\alpha=90^\circ$ drop. For the case $k+\ell=\mathbb{Z}_{even}^+$, the flow field naturally satisfies the no-flux (or no-penetration) condition on the solid support and has a CL that freely moves with fixed CA and the sessile-drop modes for this case $(\alpha=90^\circ,\Lambda=0)$ are precisely the Rayleigh modes, as required by symmetry. At this point, it is clear why Steen et al. (2019) introduced this classification scheme for a sessile drop on a solid support. Interestingly, pinning the CL for a hemispherical drop $\alpha=90^\circ$ breaks the azimuthal degeneracy of the Rayleigh spectrum (Chang et al. 2013; Bostwick & Steen 2014) and for $\alpha\neq90^\circ$, $\Lambda\neq0$ modal ordering can become complex. The $k+\ell=\mathbb{Z}_{odd}^+$ symmetry extension results in a flow field with non-zero flux across the solid support and a pinned CL. This situation can be idealized as a sessile drop connected to a fluid reservoir. In this paper, we compute the sessile-drop spectrum for the previously undiscovered $k+\ell=\mathbb{Z}_{odd}^+$ modes.

In drop-on-demand inkjet printing (Basaran, Gao & Bhat 2013; Lohse 2022), the shape of the meniscus connected to the printhead can be idealized as a 'sessile drop

connected to a fluid reservoir' where liquid is transferred from the reservoir by any number of mechanisms into the sessile drop causing pinch-off of the primary drop which deposits on the target. This is also seen in the dripping-to-jetting transition from an orifice (Richards, Beris & Lenhoff 1995; Utada et al. 2007), sometimes referred to as a capillary fountain (Schulkes 1994). The primary differences between the sessile-drop configurations shown in figure 1 are the physics that are enforced. For a sessile drop on a substrate, fluid incompressibility dictates that volume is conserved and any allowable disturbance must also respect volume conservation. In contrast, for a sessile drop connected to a fluid reservoir, volume need not be conserved because of the non-trivial flux from the reservoir. These disturbances are typically referred to as volume and pressure disturbances, respectively (Bostwick & Steen 2015). In this work, we focus on these pressure modes for the sessile drop by introducing a lumped-parameter model that relates the reservoir pressure to the drop volume change through an empirical parameter χ , which is the inverse of the acoustic compliance (Kim et al. 2011). Such lumped-parameter models are used to model the physical and electrical coupling of drop-on-demand piezoelectric inkjet printing (Gallas et al. 2003; Kim et al. 2014). In our problem, the frequency spectrum depends upon the parameters (α, Λ, χ) .

2. Mathematical formulation

Consider the sessile drop connected to a fluid reservoir shown in figure 2 with equilibrium interface defined as

$$X(s, \varphi; \alpha) = \frac{\sin(s)}{\sin(\alpha)}\cos(\varphi), \quad Y(s, \varphi; \alpha) = \frac{\sin(s)}{\sin(\alpha)}\sin(\varphi), \quad Z(s, \varphi; \alpha) = \frac{\cos(s) - \cos(\alpha)}{\sin(\alpha)},$$

$$(2.1a-c)$$

using arclength-like $s \in [0, \alpha]$ and azimuthal angle $\varphi \in [0, 2\pi]$ as generalized surface coordinates. The interface is given a small perturbation $\eta(s, \varphi, t)$ that induces a capillary-driven flow $\mathbf{v} = \nabla \psi$ defined by the velocity potential ψ which satisfies Laplace's equation on the domain D and a kinematic condition on the free surface ∂D^f ,

$$\nabla^2 \psi = 0 \quad [D], \quad \frac{\partial \psi}{\partial n} = \frac{\partial \eta}{\partial t} \quad [\partial D^f].$$
 (2.2a,b)

The pressure in the drop domain,

$$p = -\varrho \frac{\partial \psi}{\partial t} + p_{reservoir} \quad [D], \tag{2.3}$$

is the sum of the linearized Bernoulli pressure and the reservoir pressure $p_{reservoir}$ which we relate to the volume change ΔV through an empirical parameter $\bar{\chi}$,

$$p_{reservoir} = \bar{\chi} \, \Delta V = \bar{\chi} \int_0^{2\pi} \int_{\cos(\alpha)}^1 R^2 \eta \, \mathrm{d}x \, \mathrm{d}\varphi, \tag{2.4}$$

with $dx = d\cos(s)$. The pressure at the free surface ∂D^f is given by the linearized Young-Laplace equation,

$$-\varrho \frac{\partial \psi}{\partial t} + p_{reservoir} = -\frac{\sigma}{R^2} \left(2\eta + \frac{1}{\sin(s)} \frac{\partial}{\partial s} \left(\sin(s) \frac{\partial \eta}{\partial s} \right) + \frac{1}{\sin^2(s)} \frac{\partial^2 \eta}{\partial \phi^2} \right), \quad (2.5)$$

where the right-hand side is the mean curvature of the surface with the first term accounting for radial disturbances and the other two terms accounting for meridional

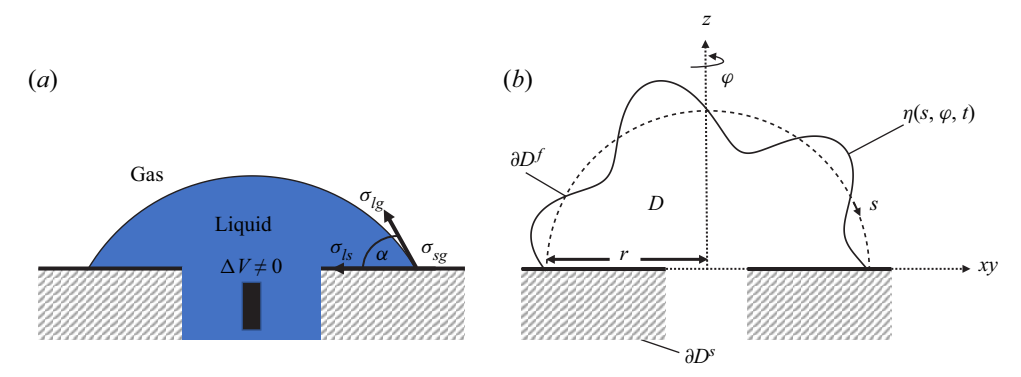


Figure 2. Definition sketch showing the (a) equilibrium sessile drop with contact-angle α given by the Young–Dupré equation and (b) disturbed shape in 2-D polar view.

and azimuthal disturbances. For reference, more details are provided in Myshkis *et al.* (1987) for an arbitrary surface. Lastly, we assume a CL condition for η that either (i) freely moves with fixed angle α or (ii) is pinned. We do not consider the more general CL speed condition with associated Davis CL dissipation (Bostwick & Steen 2014, 2016).

2.1. Reduction to operator equation

Dimensionless variables are introduced,

$$\rho^* = \rho/r, \quad \eta^* = \eta/r, \quad t^* = t\sqrt{\frac{\sigma}{\varrho r^3}}, \quad \psi^* = \psi\sqrt{\frac{\varrho}{\sigma r}}, \quad p^* = p\left(\frac{r}{\sigma}\right), \quad \lambda = \omega\sqrt{\frac{\varrho r^3}{\sigma}},$$
(2.6*a-f*)

and normal modes

$$\psi^*(\rho, \theta, \varphi, t^*) = \xi(\rho, \theta) e^{i\lambda t^*} e^{i\ell\varphi}, \quad \eta^*(s, \varphi, t^*) = v(s) e^{i\lambda t^*} e^{i\ell\varphi}, \quad (2.7a,b)$$

written in spherical coordinates (ρ, θ, φ) and parameterized by dimensionless frequency λ and azimuthal mode number ℓ are applied to the governing equations. A boundary integral approach is then applied in which the problem is mapped to the free surface (Bostwick & Steen 2014),

$$-\frac{\lambda^2}{\sin^2 \alpha} \xi - \frac{2\pi \chi}{\sin^4 \alpha} \delta_{\ell,0} \int_{\cos(\alpha)}^1 \frac{\partial \xi}{\partial n} dx = \left(2 - \frac{\ell^2}{\sin^2(s)}\right) \frac{\partial \xi}{\partial n} + \cot(s) \left(\frac{\partial \xi}{\partial n}\right)' + \left(\frac{\partial \xi}{\partial n}\right)'', \tag{2.8}$$

where $\chi = \bar{\chi} r^4 \sigma$, ' = d/ds and $\delta_{\ell,0}$ is the Kronecker delta with $\delta_{0,0} = 1$, $\delta_{\ell \neq 0,0} = 0$. Equation (2.8) is an integrodifferential eigenvalue problem in the scaled frequency λ for the harmonic function ξ , which can be recast in linear operator form,

$$M^{-1}[\xi] = \hat{\lambda}^2 K^{-1}[\xi; \ell], \tag{2.9}$$

with $\hat{\lambda} \equiv \lambda / \sin \alpha$,

$$M^{-1}[\xi] \equiv \frac{\partial \xi}{\partial n} + \frac{2\pi \chi}{\sin^4 \alpha} \delta_{\ell,0} \int_{\cos \alpha}^1 G(x, y; \ell) \, \mathrm{d}y \int_{\cos \alpha}^1 \frac{\partial \xi}{\partial n}(z) \, \mathrm{d}z \tag{2.10}$$

$$K^{-1}[\xi;\ell] = -\int_{\cos\alpha}^{1} G(x,y;\ell)\xi(y) \,\mathrm{d}y. \tag{2.11}$$

The Green's function $G(x, y; \ell)$ is defined as

$$G(x, y; \ell) = \begin{cases} \frac{1}{1 - y^2} \frac{U(x; \ell)V(y; \ell)}{W(y; \ell)}, & b < y < x < 1\\ \frac{1}{1 - y^2} \frac{U(y; \ell)V(x; \ell)}{W(y; \ell)}, & b < x < y < 1, \end{cases}$$
(2.12)

where $x \equiv \cos(s)$ and $b \equiv \cos(\alpha)$, U and V are the homogeneous solutions of the curvature operator K that satisfy the left-hand and right-hand boundary conditions, respectively,

$$U = y_1(x; \ell), \quad V = y_2(x; \ell) - \frac{\tau_2(\ell)}{\tau_1(\ell)} y_1(x; \ell), \tag{2.13a,b}$$

and W is the Wronskian of the solutions U and V. Here

$$y_{1}(x; 0) = P_{1}(x), \quad y_{2}(x; 0) = Q_{1}(x), \quad y_{1}(x; 1) = P_{1}^{1}(x), \quad y_{2}(x; 1) = Q_{1}^{1}(x),$$

$$y_{1}(x; \ell \geq 2) = (x + \ell) \left(\frac{1 - x}{1 + x}\right)^{\ell/2}, \quad y_{2}(x; \ell \geq 2) = \frac{x - \ell}{2\ell(\ell^{2} - 1)} \left(\frac{1 + x}{1 - x}\right)^{\ell/2},$$

$$(2.14)$$

where P_k^{ℓ} and Q_k^{ℓ} are the associated Legendre functions of degree k and order ℓ and the parameters τ_1 and τ_2 are related to the CL boundary conditions;

$$\tau_1^p = y_1(b; \ell), \quad \tau_2^p = y_2(b; \ell)$$
 (2.15a)

for the pinned CL disturbance (superscript p) and

$$\tau_1^f = y_1'(b;\ell) + \frac{b}{\sqrt{1-b^2}} y_1(b;\ell), \quad \tau_2^f = y_2'(b;\ell) + \frac{b}{\sqrt{1-b^2}} y_2(b;\ell)$$
 (2.15b)

for the fixed angle disturbance, sometimes referred to as the free disturbance (superscript f).

2.2. Rayleigh-Ritz method

We use a Rayleigh–Ritz procedure to compute the spectrum of (2.9) by assuming a solution series

$$\xi = \sum_{j=1}^{N} a_j \xi_j^{(\ell)}, \tag{2.16}$$

constructed from basis functions $\xi_j^{(\ell)}$ and applying inner products to generate a set of linear algebraic equations

$$\sum_{j=1}^{N} (m_{ij}^{(\ell)} - \hat{\lambda}^2 k_{ij}^{(\ell)}) a_j = 0, \tag{2.17}$$

with

$$m_{ij}^{(\ell)} = \int_b^1 \left(\frac{\partial \xi_i^{(\ell)}}{\partial n} + \frac{2\pi \chi}{\sin^4 \alpha} \delta_{\ell,0} \int_b^1 G(x, y; \ell) \int_b^1 \frac{\partial \xi_i^{(\ell)}}{\partial n} (z) dz \right) \xi_j^{(\ell)} dx dy, \qquad (2.18a)$$

$$k_{ij}^{(\ell)} = -\int_{b}^{1} \int_{b}^{1} G(x, y; \ell) \xi_{i}^{(\ell)} \xi_{j}^{(\ell)} dx dy.$$
 (2.18b)

Allowable solutions of (2.8) must necessarily satisfy Laplace's equation and allow for a non-trivial flux across the drop/reservoir boundary. This can be accomplished through judicious choice of basis functions

$$\xi_j^{(\ell)}(\rho,\theta) = \rho^j P_j^{\ell}(\cos\theta), \tag{2.19}$$

where $j + \ell = \mathbb{Z}_{odd}^+$.

The eigenfrequencies $\lambda_{k,\ell}$ have been calculated using a truncation of N=10 basis functions in the solution series (2.16) for both free and pinned disturbance. The eigenfunction $\xi_{k,\ell}$ associated with the eigenfrequencies $\lambda_{k,\ell}$ and corresponding eigenvector $a_i^{(k,\ell)}$ is given by

$$\xi_{k,\ell}(x) = \sum_{j=1}^{N} a_j^{(k,\ell)} \xi_j^{(\ell)}(x). \tag{2.20}$$

3. Results

Mode shapes can be classified using spherical harmonic terminology into zonal ($\ell=0$), rocking ($\ell=1$) and tesseral ($k\neq \ell,\ \ell\neq 0,1$) modes with $k+\ell=\mathbb{Z}_{odd}^+$ (MacRobert 1967). Typical mode shapes with associated fields (streamlines and pressure) are shown in figure 3. In what follows, we show how the frequency spectrum depends upon α, χ and the CL conditions. The motions are typically oscillatory $\lambda^2>0$, but some modes display instability $\lambda^2<0$ characterized by instability growth rate $-\text{Im}[\lambda]$. Lastly, we note that only the zonal $\ell=0$ modes depend upon χ or allow for non-trivial volume exchange between the drop and reservoir. For $\ell\neq 0$, there is a non-uniform fluid flux across the drop/reservoir boundary in the azimuthal coordinate that necessarily averages out to produce a zero net volume flux between the drop and reservoir.

3.1. Zonal
$$\ell = 0$$
 modes

Figure 4(a) plots the zonal frequencies $\lambda_{k,0}$ against the contact-angle α for $\chi=0$. This is the most stable situation. For the limiting case of the hemispherical drop ($\alpha=90^{\circ}$), the pinned modes are precisely the Rayleigh modes (1.1), as expected. The [1, 0] pinned mode has zero frequency and this is related to translational invariance which according to Noether's theorem requires a first integral of motion, as reflected in the zero-frequency motion. Deviations in either α or χ break this symmetry and result in non-zero frequency. This mode is a cousin of the 'walking instability' [1, 1] mode for the sessile drop (Bostwick & Steen 2014). Here we note the pinned (\mathcal{P}) frequencies are always larger than the free (\mathcal{F}) frequencies for fixed mode number [k, 0]. Most modes are stable and exhibit oscillations, with the exception of the [1, 0] mode which is unstable for all α for free disturbances and unstable for super-hemispherical $\alpha > 90^{\circ}$ base-states for pinned disturbances. The latter stability limit is related to the pressure turning point in the pressure–volume curve

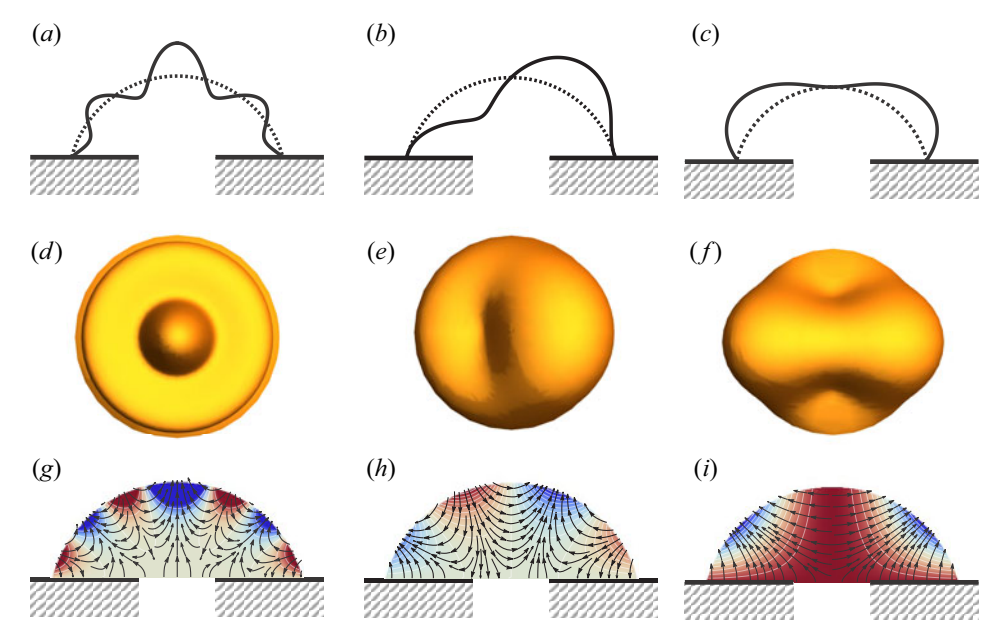


Figure 3. Mode shape $[k, \ell]$ classification plotting the interface shape in 2-D polar view (a-c) and 3-D top view (d-f) with associated fields ((g-i), streamlines and pressure contours) for typical (a,d,g) zonal [7,0], (b,e,h) rocking [4,1] and (c,f,i) tesseral [3,2] modes.

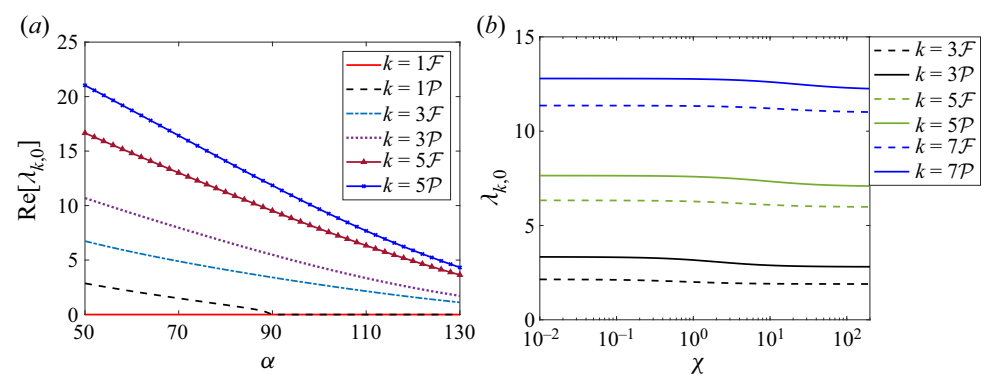


Figure 4. Zonal mode (l=0) frequency λ against (a) contact-angle α for $\chi=0$ and (b) χ for $\alpha=110^\circ$. Here $\text{Im}[\lambda]=0$ except for the [1,0] free mode and [1,0] pinned mode for $\alpha>90^\circ$.

for a pinned sessile drop (Bostwick & Steen 2015, figure 1c). Increasing $\chi > 0$ further destabilizes the [1,0] mode, but has little effect on the higher order $[k \geqslant 3,0]$ frequencies, as shown in figure 4(b). This is because the [1,0] mode is primarily responsible for volume change through vertical centre-of-mass motion.

The instability growth rate $-\text{Im}[\lambda_{1,0}]$ for the [1,0] mode increases monotonically with χ , as shown in figure 5(a). The free [1,0] mode is unstable for all (α,χ) , whereas for the pinned [1,0] mode there is a more complicated dependence. For fixed χ , there is a range of unstable α , as shown in figure 5(b). Here the instability growth rate increases as one moves away from the stability limit $\text{Im}[\lambda] = 0$ into the unstable region. Figure 5(c) plots the stability diagram for the pinned [1,0] mode in the $\chi \times \alpha$ parameter space.

D. Ding and J.B. Bostwick

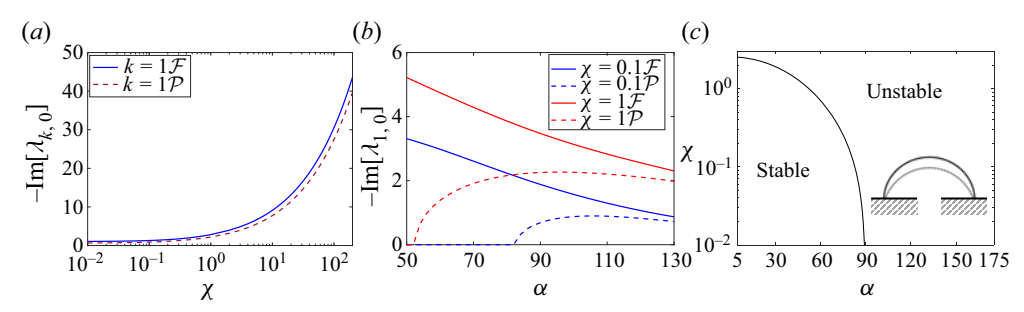


Figure 5. The unstable [1,0] mode. Instability growth rate $-\text{Im}[\lambda]$ against (a) χ for $\alpha = 110^{\circ}$ and (b) contact-angle α for $\chi = 0.1, 1$. (c) Stability diagram in the $\chi \times \alpha$ parameter space separates stable from unstable regions for pinned drops with instability shape inset. Note that free drops are unstable for all (α, χ) .

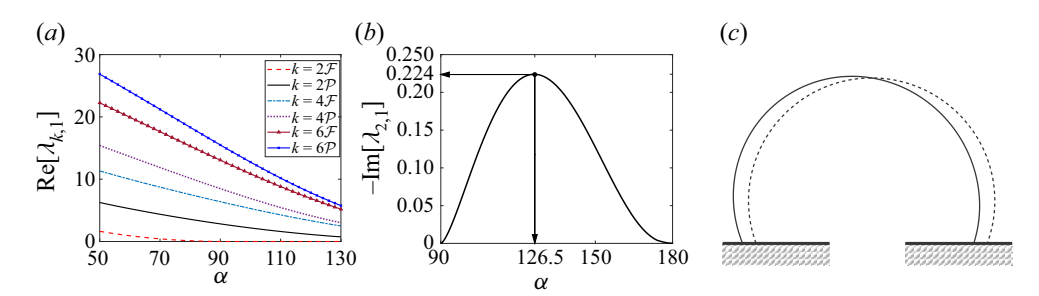


Figure 6. Rocking modes (l = 1). (a) Frequency λ against contact-angle α contrasting pinned and free modes, with $Im[\lambda] = 0$ except for the unstable [2, 1] free mode with $\alpha > 90^{\circ}$. (b) Instability growth rate $-Im[\lambda]$ for the [2, 1] free mode against contact-angle α and (c) typical unstable mode shape for $\alpha = 110^{\circ}$.

3.2. Rocking $\ell = 1$ modes

Figure 6(a) plots the rocking mode $\ell=1$ frequencies against contact-angle α , all of which decrease monotonically with increasing α . Recall that all $\ell\neq 0$ modes are independent of χ . The [2, 1] free mode exhibits instability to super-hemispherical $\alpha>90^\circ$ base-states, as shown in figure 6(b). Figure 6(c) shows the instability mode shape, which correlates with horizontal centre-of-mass motion, similar to the [1, 1] walking instability mode for the sessile drop (Bostwick & Steen 2014). The instability mechanism is similar and results from a decrease in both liquid/gas and liquid/solid interfacial areas (equivalently energies), giving rise to this motion.

3.3. Azimuthal $\ell \neq 0$, 1 modes

Figures 7 and 8 show how the azimuthal modes break the hemispherical base-state degeneracy for pinned and free disturbances, respectively. Recall for $\ell \neq 0$, there is no volume exchange between the drop and reservoir, i.e. no effect of χ on the frequencies. Pinned drops respect the Rayleigh mode degeneracy for hemispherical $\alpha = 90^{\circ}$ base-state, as required by symmetry extension. The pinned mode degeneracy is broken for $\alpha \neq 90^{\circ}$. Here for fixed polar mode number k, frequencies split lower (higher) for sub-hemispherical $\alpha < 90^{\circ}$ (super-hemispherical $\alpha > 90^{\circ}$) base-states with increasing azimuthal mode number ℓ . The degeneracy centre for the free modes shifts to lower α which also depends upon k, as shown in figure 8. For all modes, pinned and free, the frequency decreases monotonically with increasing α because of the higher inertia (volume) which biases towards lower frequency. The slope of the respective curve for fixed k decreases with

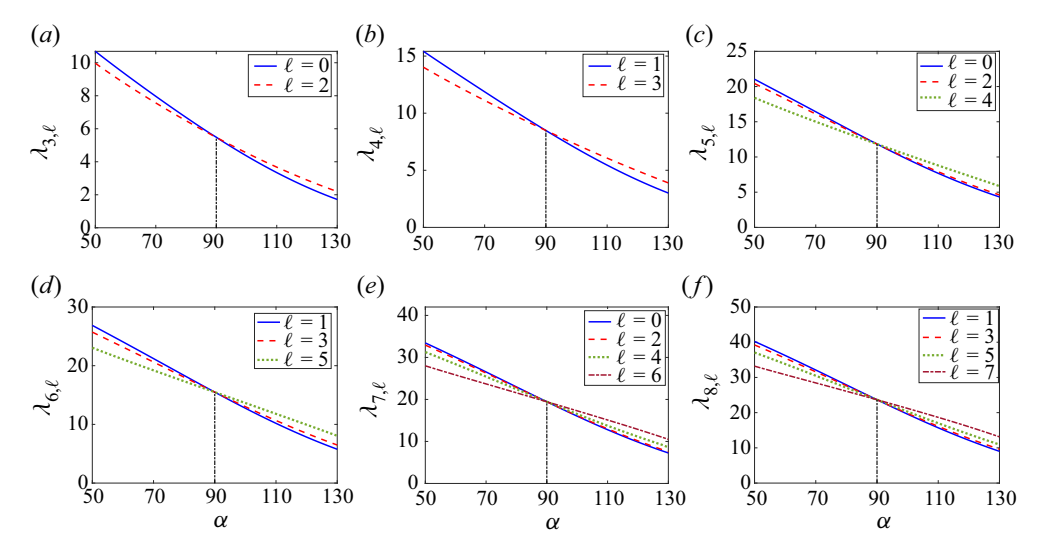


Figure 7. Oscillation frequency λ for the pinned modes against contact-angle α , as it depends upon azimuthal mode number ℓ , for polar mode number (a) k=3, (b) k=4, (c) k=5, (d) k=6, (e) k=7 and (f) k=8. Here $\chi=0$.

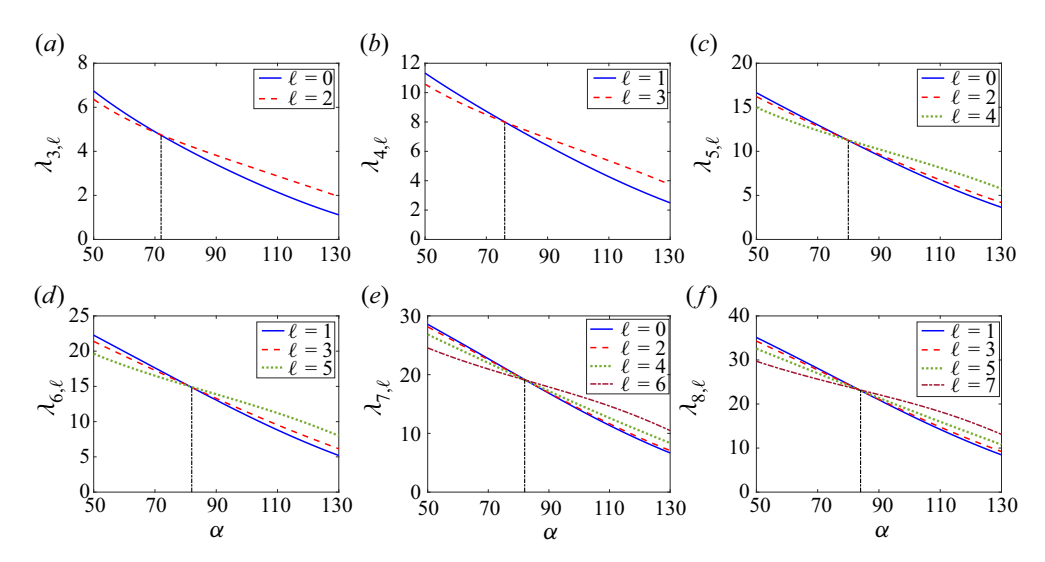


Figure 8. Oscillation frequency λ for the free modes against contact-angle α , as it depends upon azimuthal mode number ℓ , for polar mode number (a) k=3, (b) k=4, (c) k=5, (d) k=6, (e) k=7 and (f) k=8. Here $\chi=0$.

increasing ℓ and this is related to the predominantly horizontal motions for such modes which are less impacted by base-state volume. This phenomenon is discussed in more detail in Bostwick & Steen (2014, § 7.3).

4. Concluding remarks

In this work, we have computed the frequency spectrum for the pressure modes of the sessile drop connected to a fluid reservoir, as they depend upon the contact-angle α

D. Ding and J.B. Bostwick

and an empirical parameter χ relating the reservoir pressure to volume exchanged. The motions are characterized by the mode number pair $[k,\ell]$ and are related to the Rayleigh drop modes through odd symmetry extension with $k+\ell=\mathbb{Z}_{odd}^+$ required to prescribe a non-trivial flux across the drop/reservoir boundary. Prior work on sessile-drop oscillations on a rigid substrate have predicted the $k+\ell=\mathbb{Z}_{even}^+$ modes related to the Rayleigh drop modes through even symmetry extension, as required by the no-penetration condition on the solid substrate (Bostwick & Steen 2014). When combined, these two results provide a comprehensive symmetry decomposition of the Rayleigh drop modes with relationship to sessile-drop motions.

We note that our analysis was restricted to inviscid fluids and flat substrates. Viscous effects can be expected to enter this problem through the Ohnesorge number $Oh \equiv \mu/\sqrt{\varrho\sigma R}$ with μ the fluid viscosity. For millimetre-sized water drops, $Oh \approx 0.002$ and the effect of viscosity on the frequency is negligible. In inkjet printing, typical nozzle diameters are 10– $100~\mu m$ corresponding to $Oh \approx 0.01$ –0.03 implying a stronger viscous effect. Our prior work on forced oscillations of sessile drops suggests that this range of Oh would still correspond to underdamped oscillations with minimal effect on the frequency, at least for the lower order modes (Bostwick & Steen 2016). Lastly, we study the case of a sessile drop on a flat substrate, which differs from other prior works including the spherical bowl (concave) support of Strani & Sabetta (1984). Future studies could address the role of substrate curvature and viscosity.

The majority of motions predicted here are oscillatory, with the exception of the [1, 0] and [2, 1] modes, each of which exhibits instability over a specific range of contact-angles that are related to the CL boundary conditions, pinned or free. The axisymmetric [1, 0] mode is related to vertical centre-of-mass motion and the drop pinch-off seen in inkjet processes. We note the recent observation of non-axisymmetric effects in the inkjet printing process (Van Der Meulen et al. 2020). This opens up exciting possibilities for spatially resolved printing involving the pinch-off of multiple primary drops from a single print head and requiring control of surface pattern formation that precedes atomization (Vukasinovic, Smith & Glezer 2007). Alternative methods of surface patterning utilize thin films (Deblais et al. 2016). Our simple lumped-parameter model of the drop/reservoir interactions does not predict such instabilities, as could be expected, but our model could be extended to account for more complex pressure interactions between the drop and fluid reservoir that could potentially lead to the prediction of these asymmetric instabilities. Lastly, we mention that for the engineering application of reliably generating surface patterns that it may be more computationally tractable to utilize reservoir computing (Fernando & Sojakka 2003) than our analytical-based method, which is focused on the fundamental physics.

Funding. J.B.B. acknowledges support from NSF Grant CMMI-1935590.

Declaration of interests. The authors report no conflict of interest.

Author ORCIDs.

J.B. Bostwick https://orcid.org/0000-0001-7573-2108.

REFERENCES

BASARAN, O.A., GAO, H. & BHAT, P.P. 2013 Nonstandard inkjets. *Annu. Rev. Fluid Mech.* **45**, 85–113. BOSTWICK, J.B. & STEEN, P.H. 2014 Dynamics of sessile drops. Part 1. Inviscid theory. *J. Fluid Mech.* **760**, 5–38.

BOSTWICK, J.B. & STEEN, P.H. 2015 Stability of constrained capillary surfaces. *Annu. Rev. Fluid Mech.* 47, 539–568.

- BOSTWICK, J.B & STEEN, P.H. 2016 Response of driven sessile drops with contact-line dissipation. *Soft Matt.* **12** (43), 8919–8926.
- CHANG, C.-T., BOSTWICK, J.B., DANIEL, S. & STEEN, P.H. 2015 Dynamics of sessile drops. Part 2. Experiment. *J. Fluid Mech.* **768**, 442–467.
- CHANG, C.-T., BOSTWICK, J.B., STEEN, P.H. & DANIEL, S. 2013 Substrate constraint modifies the Rayleigh spectrum of vibrating sessile drops. *Phys. Rev.* E **88** (2), 023015.
- CHEBEL, N.A., RISSO, F. & MASBERNAT, O. 2011 Inertial modes of a periodically forced buoyant drop attached to a capillary. *Phys. Fluids* **23** (10), 102104.
- DAVIS, S.H. 1980 Moving contact lines and rivulet instabilities. Part 1. The static rivulet. *J. Fluid Mech.* **98** (2), 225–242.
- DEBLAIS, A., HARICH, R., COLIN, A. & KELLAY, H. 2016 Taming contact line instability for pattern formation. *Nat. Commun.* 7 (1), 12458.
- FERNANDO, C. & SOJAKKA, S. 2003 Pattern recognition in a bucket. In *European Conference on Artificial Life*, pp. 588–597. Springer.
- GALLAS, Q., HOLMAN, R., NISHIDA, T., CARROLL, B., SHEPLAK, M. & CATTAFESTA, L. 2003 Lumped element modeling of piezoelectric-driven synthetic jet actuators. *AIAA J.* 41 (2), 240–247.
- HOCKING, L.M. 1987 The damping of capillary–gravity waves at a rigid boundary. *J. Fluid Mech.* 179, 253–266.
- KIM, B.-H., KIM, S.-I., SHIN, H.-H., PARK, N.-R., LEE, H.-S., KANG, C.-S., SHIN, S.-J. & KIM, S.-J. 2011 A study of the jetting failure for self-detected piezoelectric inkjet printheads. *IEEE Sens. J.* 11 (12), 3451–3456.
- KIM, B.-H., LEE, H.-S., KIM, S.-W., KANG, P. & PARK, Y.-S. 2014 Hydrodynamic responses of a piezoelectric driven MEMS inkjet print-head. *Sensor. Actuat. A: Phys.* 210, 131–140.
- LOHSE, D. 2022 Fundamental fluid dynamics challenges in inkjet printing. *Annu. Rev. Fluid Mech.* **54**, 349–382.
- MACROBERT, T.M. 1967 Spherical Harmonics. Pergamon.
- MYSHKIS, A.D., BABSKII, V.G., SLOBOZHANIN, N.D. & TYUPTSOV, A.D. 1987 Low-Gravity Fluid Mechanics. Springer.
- RAYLEIGH, LORD 1879 On the capillary phenomenon of jets. Proc. R. Soc. Lond. 29, 71–97.
- RICHARDS, J.R., BERIS, A.N. & LENHOFF, A.M. 1995 Drop formation in liquid–liquid systems before and after jetting. *Phys. Fluids* 7 (11), 2617–2630.
- SAKAKEENY, J., DESHPANDE, C., DEB, S., ALVARADO, J.L. & LING, Y. 2021 A model to predict the oscillation frequency for drops pinned on a vertical planar surface. *J. Fluid Mech.* **928**, A28.
- SCHULKES, R.M.S.M. 1994 The evolution of capillary fountains. J. Fluid Mech. 261, 223-252.
- SHAIKEEA, A.J.D., BASU, S., TYAGI, A., SHARMA, S., HANS, R. & BANSAL, L. 2017 Universal representations of evaporation modes in sessile droplets. *PLoS One* 12 (9), e0184997.
- SHARMA, S. & WILSON, D.I. 2021 On a toroidal method to solve the sessile-drop oscillation problem. *J. Fluid Mech.* **919**, A39.
- SHARP, J.S. 2012 Resonant properties of sessile droplets; contact angle dependence of the resonant frequency and width in glycerol/water mixtures. *Soft Matt.* **8**, 399–407.
- SHARP, J.S., FARMER, D.J. & KELLY, J. 2011 Contact angle dependence of the resonant frequency of sessile water droplets. *Langmuir* 27 (15), 9367–9371.
- STEEN, P.H., CHANG, C.-T. & BOSTWICK, J.B. 2019 Droplet motions fill a periodic table. *Proc. Natl Acad. Sci. USA* 116 (11), 4849–4854.
- STRANI, M. & SABETTA, F. 1984 Free vibrations of a drop in partial contact with a solid support. *J. Fluid Mech.* 141, 233–247.
- TRINH, E. & WANG, T.G. 1982 Large-amplitude free and driven drop-shape oscillation: experimental results. *J. Fluid Mech.* 122, 315–338.
- UTADA, A.S., FERNANDEZ-NIEVES, A., STONE, H.A. & WEITZ, D.A. 2007 Dripping to jetting transitions in coflowing liquid streams. *Phys. Rev. Lett.* **99** (9), 094502.
- VAN DER MEULEN, M.-J., REINTEN, H., WIJSHOFF, H., VERSLUIS, M., LOHSE, D. & STEEN, P. 2020 Nonaxisymmetric effects in drop-on-demand piezoacoustic inkjet printing. *Phys. Rev. Appl.* 13 (5), 054071.
- VUKASINOVIC, B., SMITH, M.K. & GLEZER, A. 2007 Mechanisms of free-surface breakup in vibration-induced liquid atomization. *Phys. Fluids* **19** (1), 012104.
- WANG, T.G., ANILKUMAR, A.V. & LEE, C.P. 1996 Oscillations of liquid drops: results from USML-1 experiments in space. *J. Fluid Mech.* 308, 1–14.